J Therm Spray Tech (2024) 33:195–209
https://doi.org/10.1007/s11666-023-01690-3

ORIGINAL RESEARCH ARTICLE

Integrating State of the Art Zirconia Thermal Barriers with Ytterbium Silicate Environmental Barriers for Silicon-Based Ceramic Turbine Components

Edward J. Gildersleeve V[1] · **Emine Bakan**[1] · **Robert Vaßen**[1]

Submitted: 13 July 2023 / in revised form: 29 September 2023 / Accepted: 26 October 2023 / Published online: 30 November 2023

Abstract As gas turbine firing temperatures continue to increase for the sake of improved operating efficiency, the material's transition from Ni-based superalloy components toward ceramic matrix composites (CMCs) is concurrently in progress. Due to the complex nature of the turbine operating environment (envisaged ultrahigh temperatures, presence of water vapor, etc.), coating solutions for these CMCs are still on the forefront of design optimizations. Typically, rare-earth (RE) silicate environmental barrier coatings (EBCs) have been utilized to protect the CMCs from impinging water vapor; however, they lack the thermal insulation properties to enable continued use of simple and/or easily accessible bond coat materials (i.e., silicon). Combined thermal-environmental barrier coatings (T-EBCs) are such a multifaceted surface solution. T-EBCs have been considered in the past, but to this point have not been demonstrated to be technologically robust either due to high implementation costs or complex processing. This study utilizes and combines straightforward and well-established processes—such as plasma-sprayed 7 wt.% yttria-stabilized zirconia—to demonstrate the feasibility of MultiLayered T-EBCs comprised of zirconia-based oxides and RE silicate EBCs in a single coating. The results show that despite high thermal mismatch strains, the structures cannot only be deposited, but also in certain circumstances sustain cyclic thermomechanical loading.

Keywords atmospheric plasma spray (APS) · environmental barrier coatings (EBCs) · gas turbines · thermal barrier coatings (TBCs) · thermal cyclic properties · yttria-stabilized zirconia (YSZ)

Introduction

Modern gas turbine applications are constantly pushing toward higher firing temperatures for the sake of increased operating efficiencies (Ref 1-3). These technological goals are valid irrespective of whether hydrocarbon-based fuels or pure hydrogen is used in the turbines (Ref 4, 5). As a consequence of elevated firing temperatures and the temperature limitations of nickel-based superalloy turbine components, there are ongoing efforts to find alternative materials solutions.

In place of metallic nickel-based superalloys, ceramic matrix composite (CMC) components are the leading candidates, namely silicon carbide (SiC-SiC) CMCs. SiC-SiC CMCs not only provide enhanced temperature capabilities but also offer an improved strength-to-weight ratio, which can impart fuel savings in the aerospace sector (Ref 6-8). At present, SiC-SiC CMC components have been demonstrated in the field, and are already utilized in commercial turbine engines (i.e., GE LEAP, GE 9X, etc.) for passenger aircraft (i.e., A320, 737 MAX, etc.) (Ref 8, 9). However, it is well-established in the literature that CMCs (specifically SiC-SiC) have a number of application challenges which must be overcome. Leading these application challenges is the significant recession rates of SiC-SiC CMCs in the presence of impinging high-pressure/high velocity water vapor (Ref 6, 7, 10, 11). In addition, SiC-SiC CMCs can be subjected to significant strength loss due to oxidation. The loss in strength arises when the CMC

✉ Edward J. Gildersleeve V
e.gildersleeve@fz-juelich.de

[1] Institute of Energy and Climate Research, Materials Synthesis and Processing (IEK-1), Forschungszentrum Jülich GmbH, 52425 Jülich, Germany

oxidizes preferentially around the SiC fibers, thereby embrittling the interface between the fiber and the matrix (Ref 12-14).

These two major CMC issues of water vapor stability and volatilization along with oxidation-induced embrittlement have driven research into surface solutions to enable their use as high-temperature (rotating) turbine components. With respect to the oxidation challenge, certain localized regions of the CMC might have appreciable concentrations of boron, which can change the chemistry and microstructure of the CMC's thermally-grown oxide (TGO) scale (Ref 15). More et al. showed for a representative SiC-SiC CMC there can be as much as four distinct oxide species that form during thermal cycling (Ref 11). Most notably, however, More et al. showed the SiC-SiC CMCs are prone to form porous SiO_2 TGO scales, which can allow for further ingression of oxidative species to accelerate attack (Ref 11).

Similar to the case of Ni-based components, one mitigation strategy against deleterious CMC oxidation would be to utilize a protective overlay coating that forms a dense TGO scale. For instance, pure silicon, which forms dense SiO_2 under prolonged thermal exposure, has been considered as a coating material in the past (Ref 16, 17). However, representative turbine environments (specifically downstream, starting at the combustor) have a non-negligible concentration of water vapor. Consequentially, the presence of water vapor will accelerate SiO_2 TGO consumption due to reaction and volatilization into Si(OH)x gaseous species, which then exposes fresh Si and can inspire regrowth of new SiO_2 (Ref 10, 18). Therefore, dense (gas-tight) environmental barrier coatings (EBCs) have been heavily researched over the last decades as a means to isolate the CMC-Si-SiO_2 system from incident water vapor (Ref 16, 19-24).

While certain EBC materials are well-known for their potential to limit water vapor attack, there are still inherent design challenges for the entire turbine coating system which have to be contemplated. The low melting temperature of silicon (relative to the envisaged modern turbine firing temperatures) implies the need for some form of thermal protection to continue using this material (Ref 1-4). Alternative materials to silicon have been proposed, but to this point have been shown in the literature to have certain weaknesses which must be overcome before replacing silicon (Ref 25-27).

Concurrently, most candidate EBC materials (that are either in use commercially or those which are being considered) do not have the same inherently low thermal conductivity as contemporary thermal barrier materials. Therefore, the only options to get the necessary through-thickness temperature drop to allow the use of silicon (or silicon-like materials) would be to either make the EBC quite thick (i.e., > 1 mm) or implement increased backside cooling (Ref 16, 22, 24, 28-30). Both of these options are undesirable; on the one hand, increased backside cooling will lead to efficiency losses in the turbine. Likewise, highly thick EBC layers can be prone to premature through-thickness segmentation cracking and delamination/spallation due to the increased available elastic energy in the coating—which will then lead to undesired infiltration of water vapor toward the SiO_2 TGO (Ref 31-35).

These concurrent yet conflicting design and application considerations in modern turbine engines are what then drive the need for an alternative, novel surface solution which can simultaneously provide thermal insulation and water vapor protection. So-called thermal-environmental barrier coatings (T-EBCs) have been considered in the past literature; however, they typically have utilized complicated multiphase oxides, expensive processing techniques, and generally have disregarded the use of silicon entirely (Ref 17, 36-38). In this paper, an investigation was taken in studying the efficacy of using one process—atmospheric plasma spraying (APS)—to deposit MultiLayered T-EBCs onto silicon-bond-coated SiC substrates. For this study, only traditional thermal/environmental barrier oxides with a deep history of published literature such as yttria-stabilized zirconia (YSZ), gadolinium zirconate (GZO), and ytterbium disilicate ($Yb_2Si_2O_7$, YbDS) were utilized. YSZ was chosen here given its wide acceptance both in published literature and in the industry as an omnipresent thermal barrier material. However, there are of course limitations in terms of phase stability and resistance to turbine-ingested foreign debris at these envisioned high firing temperatures for traditional YSZ, therefore GZO was also considered as a candidate TBC material (Ref 39-42).

Such combinations of YSZ/GZO with YbDS in a single coating stack have yet to be introduced in the literature. This is likely due to the large thermal expansion (CTE) mismatch strains that would exist in a YSZ/YbDS/Si/SiC-SiC system. Clearly, given this CTE-driven challenge, microstructural control and optimization of each layer in the T-EBC system to minimize the driving forces for failure is mandatory. It has been shown in previous studies that by optimizing the microstructure, heterogeneous MultiLayer structures of different TBC oxides can be deposited—and in some cases outperform their single-layer counterparts (Ref 41, 43-46). The lessons learned from these studies were then adopted here, with the goal of studying the effect of modulating the TBC portion of the T-EBC in terms of microstructure (i.e., standard porous YSZ vs. a porous/dense vertically cracked double-layer TBC). In addition, because of the somewhat unconventional approach of depositing directly onto the EBC, the question of whether or not to unconventional approach of depositing directly onto the EBC, the question of whether or not to crystallize the EBC before TBC deposition arose. Crystallization of the EBC is a given necessity, considering all (traditionally deposited) plasma-sprayed EBCs are amorphous on deposition and require a post-deposition annealing to crystallize (Ref 21, 24, 47). However, to this point in time, there have been no studies that directly evaluate whether or not it is significant to crystallize the EBC layer before TBC deposition in a T-EBC. The results from this study will show two important findings that should contribute toward the community's understanding of what is defined here as the 'feasibility' of such a zirconia-based/rare-earth disilicate T-EBC. First, despite the CTE incompatibility between the TBC and EBC layers, it will be demonstrated that it is nonetheless possible to deposit MultiLayered, Multicomponent T-EBCs while retaining microstructural integrity. Furthermore, it will be shown that some of these T-EBC structures can also sustain repeated thermomechanical cycling.

Experimental Methods

Deposition of the T-EBC MultiLayers

For the deposition of the T-EBC MultiLayers, all of the layers were deposited using the APS process. For the silicon bond coat and YbDS EBC layer, a cascaded arc plasma torch (TriplexPro 210, Oerlikon Metco, Wohlen, Switzerland) was utilized. Meanwhile, for the deposition of YSZ and GZO layers, a standard DC plasma torch (F4MB, Oerlikon Metco, Wohlen, Switzerland) was used. These separate plasma spray processes and coatings were chosen as components of the MultiLayer because they have been utilized in a number of previously published works which examine their thermophysical properties, functional performance, and reproducibility. A summary of the general processing conditions is shown in Table 1, and more details can be found in these previous studies (Ref 48-50). Feedstocks utilized were a mixture of commercial-grade thermal spray powders and commercial powders that were manually screened to reduce the number of large agglomerates. These details are also provided in Table 1. All coatings were sprayed onto 25 × 25 × 3 mm Hexoloy-SA dense SiC tiles (Saint-Gobain Technical Ceramics, Niagara NY) that were gritblasted with F150 SiC grit at a pressure of approximately 4 bar. Every layer in Table 1 was sprayed using a similar toolpath (notwithstanding different standoff distances) and the same preheating approach. For preheating, the samples were exposed to the plasma torch prior to powder feeding by rastering across the surface until a steady-state temperature of around 300 °C was reached (measured by infrared pyrometry, 4 M8 pyrometer (λ = 13 µm) [Land Instruments GmbH, Leverkusen, Germany]). Then, deposition at the parameters listed in Table 1 is carried out.

For the thermal barrier portion of the T-EBCs, three variants were studied. These three thermal barrier permutations comprised of a standard porous (15-20% porosity, (Ref 48)) YSZ; the same porous YSZ + segmented YSZ; and porous YSZ + segmented GZO. These three TBC permutations were sprayed atop either as-sprayed (amorphous; hereafter referred to as 'amorphous on deposition') or heat treated (hereafter 'crystalline') YbDS, to evaluate if the crystallinity of the underlying EBC had any effect on the bonding/adhesion between the TBC and the EBC. The coating methodology is summarized in Table 2. For crystallizing the YbDS EBC, a two-step annealing treatment as described in past literature was utilized (Ref 50). In all cases, the total thickness of the T-EBC MultiLayer was constrained to be between 350 and 400 microns thick.

Microstructural Characterization

After deposition, coatings were embedded in a 2-part epoxy resin by vacuum impregnation (EpoFix, Struers GmbH, Willich Germany). Then, the embedded coatings

Table 1 Summary of processing conditions used to deposit the T-EBC layers (Ref 48-50)

Layer	Feedstock	Feed rate, gram min^{-1}	Ar, slpm	H2/He§, slpm	Current, Amps	Standoff distance, mm	Net power, kW
Silicon*	Oerlikon 4810	30	50	0	450	100	23
$Yb_2Si_2O_7$*	Oerlikon 6157x	23	46	4§	325	90	17
YSZ Porous^{+}	Oerlikon 204NS	30	47.5	6	550	150	19
YSZ Segmented^{+}	Amdry 6643	30	65	11	550	60	24
GZO Segmented^{+}	Höganas Amperit 837	30	65	11	550	60	24

*TriplexPro^{TM} Plasma Torch; + F4MB Plasma Torch; xScreened to nominal 10-40 µm PSD; §symbol indicates the flow rate was helium

Table 2 Summary of the T-EBC samples considered in this study

Set	$Yb_2Si_2O_7$ Crystallinity	Thermal barrier layer 1	Thermal barrier layer 2
A	Amorphous / As sprayed	YSZ Porous	N/A
B	Amorphous / As sprayed	YSZ Porous	YSZ Segmented
C	Amorphous / As sprayed	YSZ Porous	GZO Segmented
D	Crystalline / Heat Treated	YSZ Porous	N/A
E	Crystalline / Heat Treated	YSZ Porous	YSZ Segmented
F	Crystalline / Heat Treated	YSZ Porous	GZO Segmented

were cross-sectioned using a diamond high-speed saw (Accutom, Struers GmbH Willich Germany). One half of the specimen was then re-mounted by vacuum impregnation and polished using standard metallographic methods for cross-sectional analysis of the as-sprayed systems. The other half of the mounted/sectioned specimens were then heat-treated in a muffle furnace (Carbolite Gero CWF1300, United Kingdom) at 800 °C for 4 hours. This was done to vaporize the remnant epoxy and bring the coating back to an unmounted state. It has been shown in the past literature that this vaporization process induces no significant damage to thermally-sprayed coatings; and an equivalent assessment was carried out in this study to confirm the same (Ref 51).

For viewing of all cross sections, a LaB6 cathode scanning electron microscope (SEM) was utilized (ZEISS EVO15, Carl Zeiss Inc., United Kingdom) equipped with an energy-dispersive spectroscopy (EDS) detection system (Oxford UltiMax100, Oxford Instruments, United Kingdom). Cross-sectional viewing and EDS analysis was carried out at 20 kV accelerating voltage in the backscatter mode.

The surface topography and roughness of the as-sprayed and annealed coatings were characterized by a non-contact profilometer using a confocal white light sensor with a vertical resolution of 0.035 µm (Cyber Scan, CT350T, Cyber Technologies, Munich, Germany).

Micro-Raman spectroscopy was carried out using a Renishaw InVia Raman microscope with a solid-state 50mW 532 nm excitation laser and 2400 lines per mm grating. To avoid any laser-induced damage to the specimen, separate investigations to determine a safe laser power level for sufficient Raman excitation were carried out. Ultimately, a laser power of 10 percent ($\sim$5mW) was chosen. Raman mapping was carried out by using an automated dynamic focus function within the microscope software (WiRE 5.1, Renishaw). Spectra were collected in a 90×50 um^2 area at a collection time of one second per spectrum and a step size of 1 micron. The 14,000 spectra were then processed and analyzed within the WiRE 5.1 software by using a statistical least squares component fitting algorithm to generate the Raman map.

Thermomechanical Testing

The remaining half-samples after epoxy vaporization were then taken again to a muffle furnace (Carbolite Gero, CWF1300, United Kingdom) and thermally cycled in air at 1300 °C for 20-hour thermal cycles. Heating was done at 10 K /min, and cooling was done in-furnace to room temperature at 10 K /min. After each thermal cycle, the specimens were visually inspected for obvious signs of spallation/cracking/delamination. Samples were considered to have failed if greater than 20% of the surface area of the coating showed signs of delamination/spallation. After 10 thermal cycles (200 hours thermal exposure), all remaining specimens were removed from the furnace and then mounted/sectioned/polished as described previously for viewing the thermally-cycled microstructure. Due to the limitations in number of samples, it was not possible to extract one of each of the amorphous-on-deposition T-EBCs after the first thermal treatment to evaluate any changes in structure after crystallization.

Results and Discussion

As-Deposited Microstructural Evaluation

Figure 1 shows the as-deposited microstructures of the T-EBCs fabricated in this study. From the Figure, there are clear differences at the interface between the TBC and EBC layers. For instance, when comparing Fig. 1(a) with Fig. 1(d), there is a clear separation between the porous YSZ and crystalline YbDS layers in Fig. 1(d) (indicated by an arrow) that is not evident in Fig. 1(a) (amorphous YbDS). These differences in bonding when the TBCs are sprayed on amorphous versus crystalline YbDS are consistent for all the MultiLayers considered in this study. In the cases where the topmost TBC layer(s) were deliberately sprayed with segmentation cracks, it seems these cracks propagated further into the porous YSZ layers (Fig. 1b, c, e, f). Interestingly, the propagation of segmentation cracks does not seem to continue into the EBC layer when the YbDS coating is crystallized before deposition of the TBC (Fig. 1e, f).

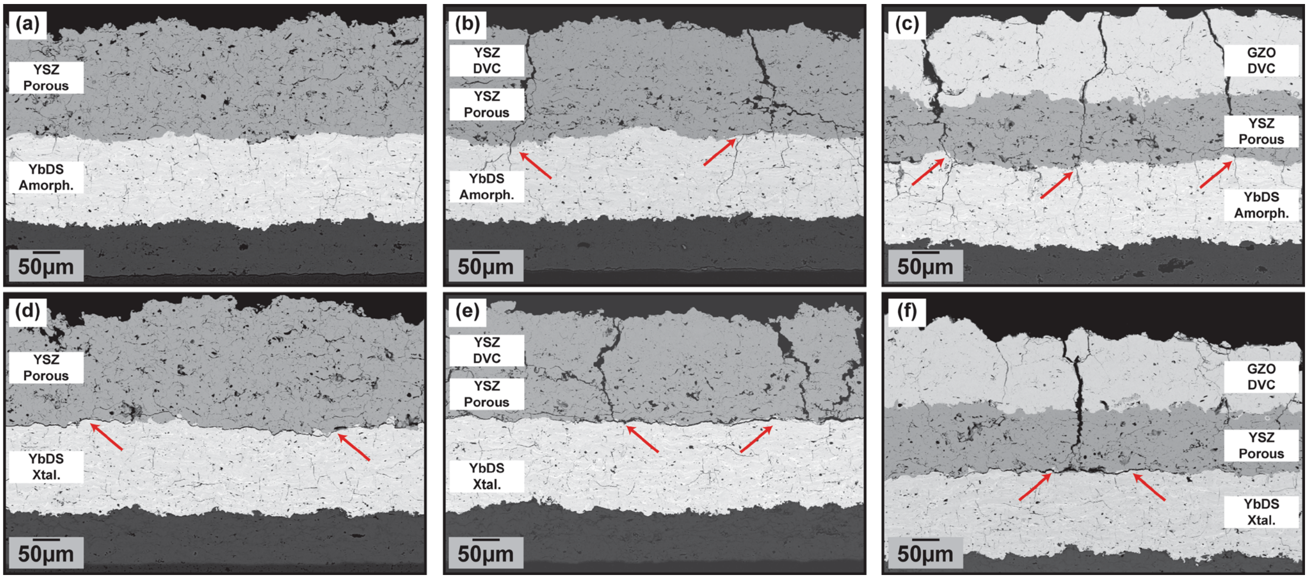

Fig. 1 As-deposited microstructures (a, b, c) of the T-EBCs deposited on amorphous ytterbium disilicate. (d, e, f) show the as-deposited T-EBCs atop crystalline ytterbium disilicate. Arrows indicate regions where either segmentation cracking propagated into the EBC layer (b, c) or local delamination occurred between the TBC and EBC (d, e, f)

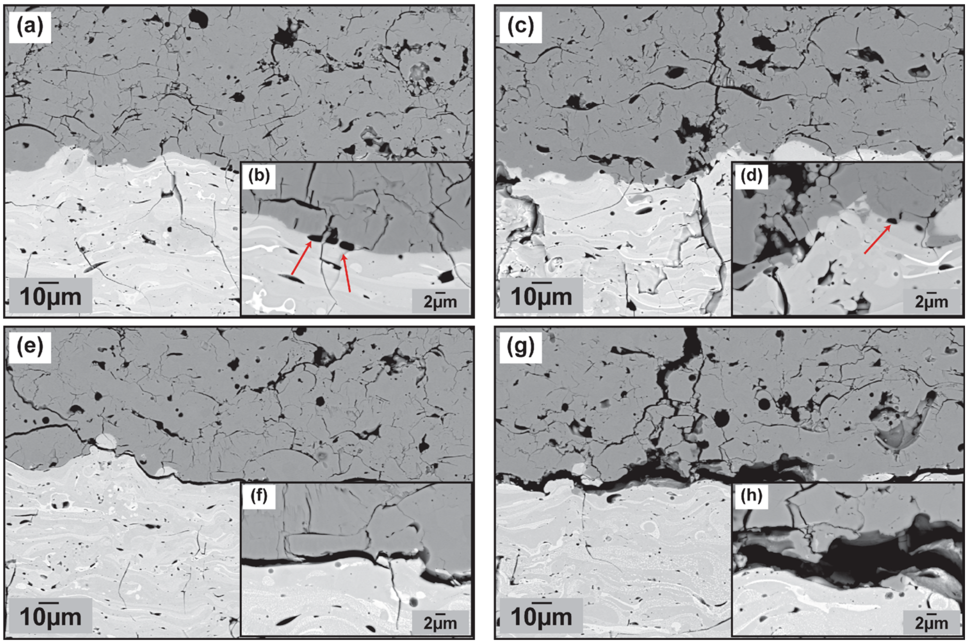

Fig. 2 High-magnification images of (a, c) the YSZ/YbDS (amorphous) interface for T-EBC A and C, respectively and (e, g) the YSZ/YbDS (crystalline) interface for T-EBC D and F, respectively. The inset images show even higher magnification images of the same. Arrows indicate regions where interfacial voids unique to both coating microstructures have formed

Figure 2 shows high-magnification images of the TBC/EBC interfaces shown in Fig. 1. From Fig. 2, it is clear that the YSZ/YbDS interface is heavily influenced by the crystallinity of the underlying EBC layer. Interesting to note is it seems when the YSZ is deposited onto amorphous YbDS, voids coalesce and form at the TBC/EBC interface. This is indicated by the arrows in Fig. 2(b) and (d). On the other hand, when the YSZ layer is deposited on crystalline YbDS, these interfacial voids are much less frequently found. Furthermore, from the similarities between Fig 2(e) and (g), it is clear that the separation of the TBC and crystalline EBC occurs directly after the deposition of the porous YSZ layer.

If there is some preexisting interfacial separation, then as the segmentation cracks propagate from the DVC TBC to the porous TBC and then finally toward the EBC, the reduced interface toughness due to the pre-separation should be the dominating factor (Ref 31, 33, 35, 52). As shown by Hutchinson, for the problem of crack deflection versus propagation at an interface of two discrete materials,

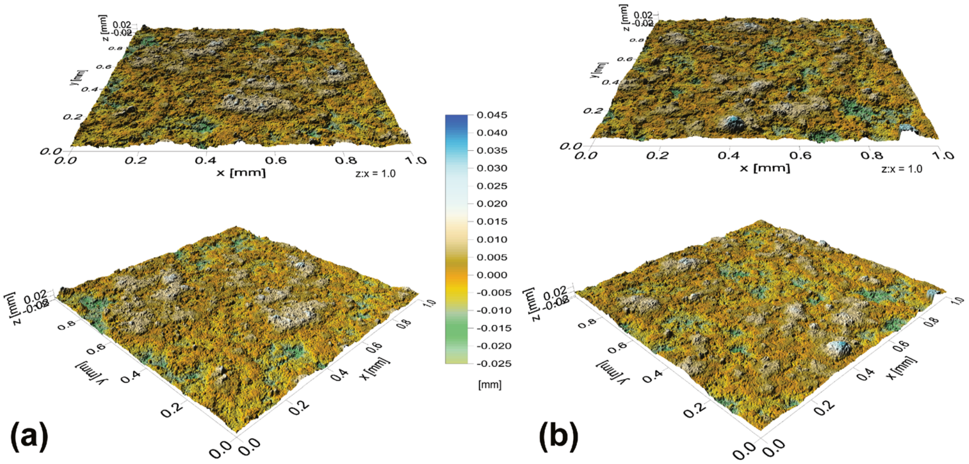

Fig. 3 Surface topography images of the amorphous (a) and crystalline (b) ytterbium silicate EBC coatings

the necessary condition for the crack to be deflected into the interface is when $\frac{G_c - \mathrm{int}(\psi)}{G_c^{(1)}} < \frac{G_{\mathrm{deflection}}}{G_{\mathrm{propagation}}}$ where G is the energy release rate (Ref 52). In the case of a pre-separated interface (prior to segmentation crack propagation), the $G_c - \mathrm{int}(\psi)$ parameter should approach zero, suggesting segmentation crack deflection (or arresting) should occur—which is consistent with the experimental observations. One can also consider the differences in the apparent $G_c^{(1)}$ between amorphous and crystalline YbDS. In the case of an amorphous YbDS layer, it is well-known that the material does not experience the same extent of microcracking events as polycrystalline ceramics during quenching (Ref 20, 21, 24, 53). Without these stress-relieving microcracks, the amorphous YbDS is expected to retain an appreciable amount of the tensile quenching stresses during solidification (notwithstanding viscosity-induced creep relaxation of the amorphous material). Therefore, as a segmentation crack approaches a residually-tensile-stressed glass-ceramic, the apparent $G_c^{(1)}$ of this amorphous YbDS is likely to be less than a crystalline YbDS—which has undergone thermal treatment, creep relaxation, and due to CTE mismatch strains, should be, by contrast, in residual compression. Regardless of whether this is a contribution of the $G_c - \mathrm{int}(\psi)$ or the $G_c^{(1)}$, or both, the net effect is clearly shown in Fig. 2(g), wherein the advancing crack front from the segmentation crack stops some micrometers above the YSZ/YbDS interface. Subsequent sections of this paper will focus on characterizing and attempting to ascertain a rationale as to what may contribute to this observed difference in interfacial bonding.

Characterization of the YSZ/YbDS Interface

Surface Roughness of Amorphous Versus Crystalline YbDS

It is well-known within the thermal spraying community that the adhesion of a thermally-sprayed material is usually governed by the mechanical interlocking of the individual solidifying droplets (i.e., splats) (Ref 53, 54, 55). The quality and strength of this mechanical interlocking (i.e., adhesion strength) has classically been attributed to factors such as surface roughness, the presence (or lack thereof) of contaminants, etc. (Ref 56). By extension, a typical explanation for poor layer bonding is due to a reduced/low adhesion strength at the interface. Thus, it was necessary to investigate whether the TBC/EBC separation observed in Fig. 1 and 2 could stem from reduced adhesion strength due to surface changes (i.e., during YbDS crystallization). The surfaces of as-deposited (amorphous) and heat treated (crystalline) YbDS coatings were analyzed with white light interferometry to study the change (if any) in the surface roughness of the coating after crystallization.

Table 3 Surface roughness parameters of the amorphous and crystalline ytterbium silicate EBCs considered in this study

YbDS crystallinity	Ra,um	Rq, um	Rz, um
Amorphous	3.08 ± 0.04	4.12 ± 0.06	20.4 ± 0.42
Crystalline	3.03 ± 0.04	4.05 ± 0.06	20.2 ± 0.45

Figure 3 shows the surface topography images of the two YbDS coatings. From the Figure, there are no discernible differences in surface characteristics between the specimens. Line scans of the surface topography showed similar evidence. Furthermore, roughness parameters Ra, Rq, and Rz were extracted from the interferometry data, and are shown in Table 3. The quite similar roughness parameter values in the Table corroborate with the qualitative lack of discernable microstructural differences in Fig. 3 before and after crystallization for the YbDS EBCs. These results suggest that the observed differences in TBC/EBC interfacial bonding from Fig. 1 and 2 must come from an alternative source beyond mere differences in mechanical interlocking, which was explored further.

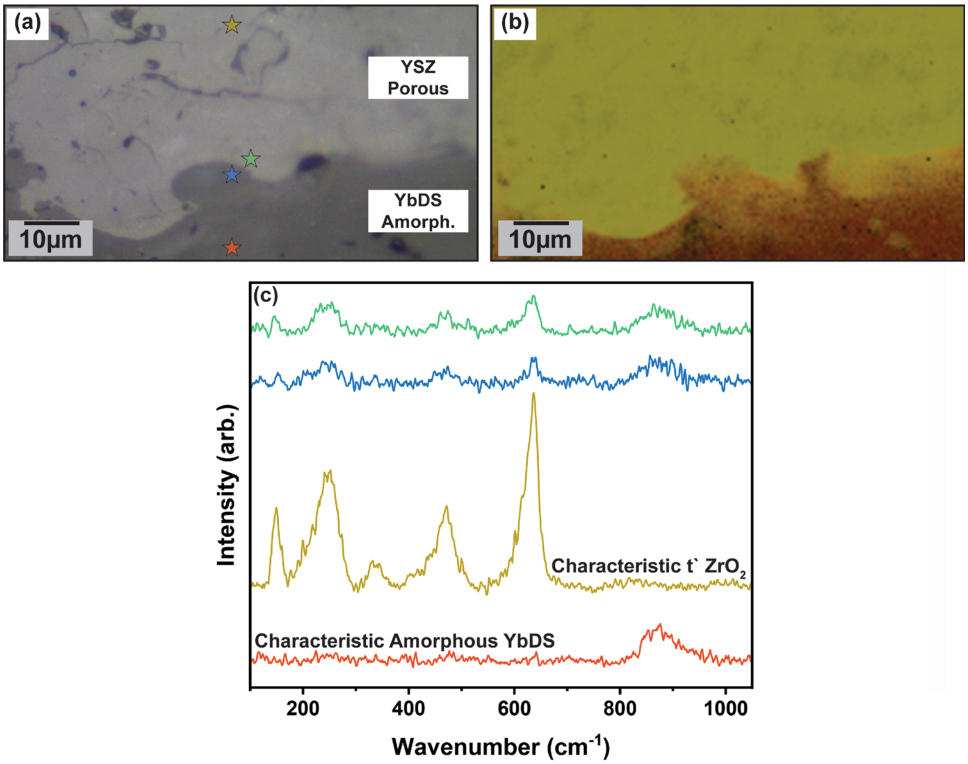

Fig. 4 (a) Optical micrograph image of a cross-sectional location which was examined with Raman Spectroscopy. (b) Raman map of [yellow] t' ZrO_2 and [red] amorphous YbDS. (c) Raman spectra of four representative locations (marked as stars in (a)) in the cross section. The characteristic spectra of t' ZrO2 and amorphous YbDS used to fit the entirety of the map data in (b) is plotted. In addition, two spectra from locations at the YSZ/YbDS interface are shown

Chemical and Phase Analysis of the YSZ/YbDS Interface

Figure 4 shows the interface of Sample A from Table 2 when analyzed using Raman Spectroscopy. From the collection of several thousand Raman spectra, a Raman map was generated by fitting the data against two representative/characteristic spectra far away from the YSZ/YbDS interface. These characteristic spectra are shown in Fig. 4(c). The Raman spectra in the APS YSZ coating are consistent with expectations for t' YSZ (Ref 57, 58). The high crystallinity and phase purity of APS YSZ TBCs is also consistent with what is observed in the Raman spectrum as sharp, well-defined peaks. Conversely, because the YbDS is predominantly amorphous, the Raman spectrum in the YbDS coating is almost devoid of peaks, which is consistent with expectations (Ref 59, 60). Nevertheless, one distinct broad peak can be seen for the amorphous YbDS between 850 and 950 cm^{-1}, which is unique from the characteristic t' ZrO2 spectrum shown. It was then possible to fit all Raman spectra collected against these two reference spectra and determine qualitative differences in phase concentrations within the microstructure. From the Raman map in Fig. 4(b), it might be suggested that ZrO2/YSZ could be present in the amorphous YbDS layer (and vice versa). However, spatial resolution limitations in the Raman microscope are of concern here; and thus, the results presented can only be used as a qualitative suggestion toward the possibility of an interexchange (or intermixing) between species.

SEM/EDS analysis was then utilized in an attempt to characterize this interface and study the possibility of interexchange of species within the regions of interest more rigorously. A representative location in one of the T-EBC samples is shown in Fig. 5(a). From Fig. 5(b), an elemental line scan was carried out starting within a YbDS particle and iteratively stepping by 0.5 μm into the YSZ coating (indicated by a dashed line in Fig. 5a). From the line scan data, it appears that within the YbDS particle (in the left-most portion of the BSE image) there is an area that shows Yb depletion and Zr enrichment. In addition, far from any YbDS material (toward the center of the image), it also seems that the bright regions within the YSZ coating (that seem to outline the grain boundaries) are Yb-rich regions (indicated by the blue star in Fig. 5a). An individualized EDS point scan at the blue star in Fig. 5(b) was taken, where there is clear excitation of the Yb-M line (Fig. 5c). The results from Fig. 5 are shown as representative results—that is, equivalent results were found in Samples A-C at similar locations around the YSZ/YbDS interface, irrespective of the top TBC microstructure(s). Interestingly, these trends (and suggestions of species interexchange) were not observed when the YSZ was deposited onto the crystalline YbDS EBC. To rule out contributions from excitation volume, Monte Carlo simulations using JEOL's Electron Flight Simulator software package were

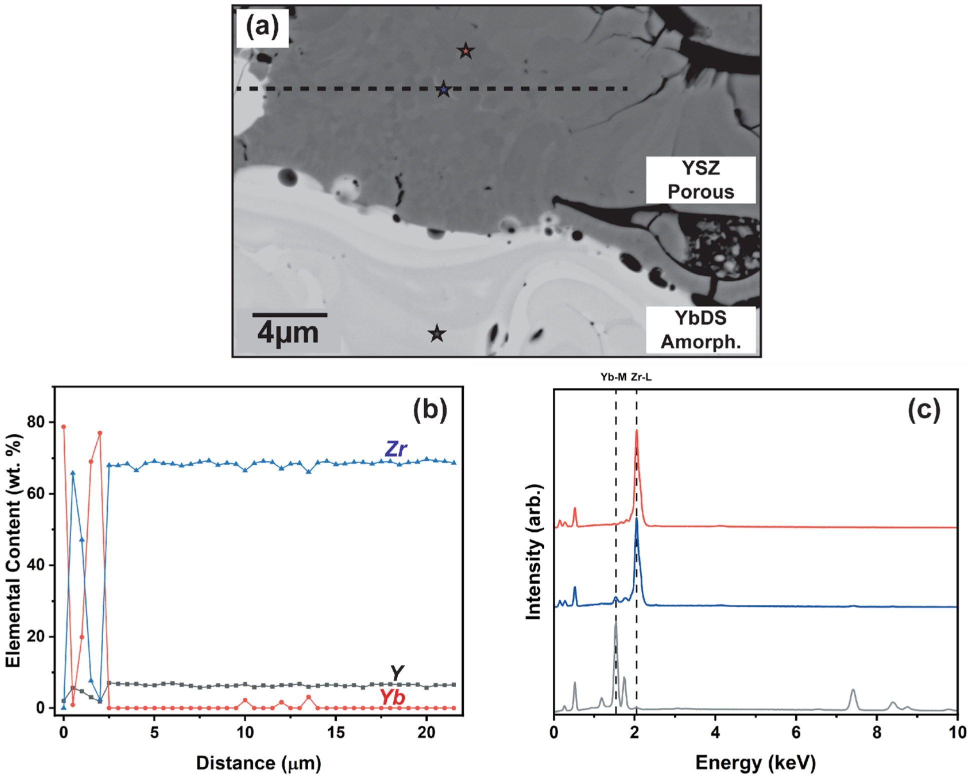

Fig. 5 (a) Cross-sectional BSE image of a reference location in Sample B [YbDS amorphous on deposition] at the YSZ/YbDS interface. The dashed line indicates the region where an EDS line scan was taken—the data for which is shown in (b). The starred regions indicate locations where single point scans were taken—the data for which is shown in (c). In (c), the Yb-M and Zr-L line locations are indicated by dashed lines

Table 4 Thermal cycling performance summary of the T-EBCs considered in this study

Set	Furnace cycle life (cycles)	Failure condition
A [YbDS Amorphous-on-deposition]	10	No macroscopic failure
B [YbDS Amorphous-on-deposition]	10	No macroscopic failure
C [YbDS Amorphous-on-deposition]	10	No macroscopic failure
D [YbDS Crystalline-on-deposition]	2	> 30% surface area spallation after 2 cycles
E [YbDS Crystalline-on-deposition]	0	Spallation occurred after epoxy vaporization treatment
F [YbDS Crystalline-on-deposition]	0	Spallation occurred after epoxy vaporization treatment

After ten 20-hour thermal cycles, the test was terminated.

carried out, and it was found that the Yb-M signal should be virtually undetectable through ZrO2 under the given SEM operating conditions used in this study.

Thermomechanical Cycling of MultiLayered T-EBCs

Table 4 summarizes the FCT findings for the six sample sets in this study. Interestingly, for the T-EBCs wherein TBCs were sprayed onto amorphous YbDS (Samples A-C), all samples showed no signs of macroscopic failure/spallation after the full 200 hours of FCT. However, in the case of the T-EBCs wherein the YbDS was crystalline before deposition of the TBC layer(s) (Samples D-F), the thermal cyclic durability was markedly poorer.

Microstructural Analysis of the Single-Layered Porous YSZ on YbDS

The representative cross-sectional micrographs of the porous YSZ on amorphous and crystalline YbDS samples (Sample A and Sample D from Table 2 and Table 4, respectively) after FCT are shown in Fig. 6. From the Figure, it is evident that in both cases, the porous TBCs experienced significant thermomechanical stresses during the thermal cycling—such that new through-thickness vertical cracks formed to release the stored energy in the

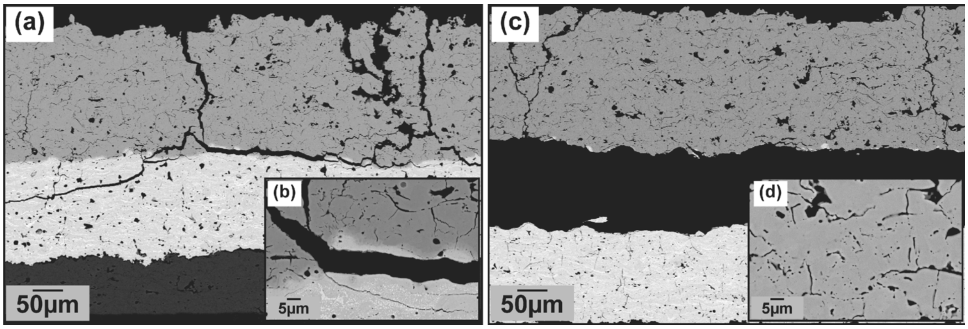

Fig. 6 FCT cross-sections of (a, b) Sample A [YbDS amorphous-on-deposition; after ten 20-hour cycles] and (c, d) Sample D [YbDS crystalline-on-deposition; after two 20-hour cycles] from Table 2. High-magnification images near the YSZ/YbDS interface are shown in both cases

system (Ref 31, 33, 35). These stress excursions are anticipated to be even more extreme for Sample A—because the amorphous YbDS layer has yet to face the substantial strains induced during crystallization (Ref 23, 24, 47, 50, 61, 62). In the case here, the crystallizing YbDS is further constrained not only by the Si + SiC, but also by the overlaying YSZ layer—which has a higher thermal expansion coefficient. This type of unique constrained crystallization and phase transformations might induce even more stress into the EBC, although the effect could be somewhat limited by the SiC substrate. It was nevertheless surprising to find there were no locations along the length of Sample A where extensive TBC/EBC delamination was observable.

Furthermore, it seems (in general) that the crack opening displacements of these newly-formed vertical cracks are larger for Sample A (where the YbDS was amorphous on deposition) than in the case of Sample D (YbDS crystalline on deposition), which could also be attributed to the higher transient stress excursions during initial YbDS crystallization and phase transformations.

On the other hand, it is equally possible that the larger crack opening displacements are a result of the longer cycling time (Table 4). Figure 6(d) shows even after only two thermal cycles, the lamellae and microcracks within the YSZ TBC are already beginning to coalesce and sinter. With a longer cycling time at 1300 °C, it is plausible to consider the YSZ TBC sintered even further (before sustaining the cracking damage seen in the Figure). Prolonged sintering would thereby increase the stiffness of the YSZ, which would then (under similar thermomechanical strains) increase the stored energy in the coating (Ref 51). As the stored energy continues to increase, the propensity for large-scale cracking also increases. This could contribute to the observed differences in the crack opening displacement. Given the limited number of samples and complex mechanistic interplay between the sintering, cracking, and crack opening in these systems, quantification by image analysis of any of these microstructural changes is too ambiguous with the available data from this study. Future work could be directed toward more deliberate and interrupted thermal cycling to assess exactly how and when sintering and through-thickness cracking can occur for each of the T-EBC microstructures presented here.

Figure 6 also demonstrates the influence of YbDS crystallinity on the tendency for cracking or delamination to occur. In the case of the T-EBC with an amorphous-on-deposition YbDS (Sample A), the through-thickness vertical cracks in the TBC appear to have bifurcated either along the YSZ/YbDS interface or into the YbDS EBC directly. This result is consistent with what has been observed recently by Deijkers et al., wherein for HfO_2/YbDS T-EBCs, crack bifurcation along the TBC/EBC interface was observed (Ref 63). Here, the authors interpret the compressive stress state of the YbDS layer due to the thermal expansion mismatch will limit crack propagation to only be able to occur along this TBC-EBC interface. The results from Fig. 6 somewhat support this; however, the Deijkers et al. study conducted all their depositions in a 1200 °C furnace to enhance TBC-EBC bonding. Here, we are depositing at normal deposition temperatures of around 400-500 °C, and it is obvious from the Fig. 6 that the YSZ on crystalline YbDS interfacial bonding is significantly poorer. Therefore, it seems under more traditional APS deposition methodologies, the crack bifurcation is much more influenced by the TBC-EBC interfacial bond strength.

Nevertheless, despite these cracking events, the T-EBC A did not visually appear to be spalled during the thermal cycling. The surprising adherence between the YSZ and YbDS through prolonged thermomechanical cycling further supports the hypothesis that there is a significantly higher TBC/EBC interfacial fracture toughness when depositing directly onto amorphous YbDS (as discussed in Section As-Deposited Microstructural Evaluation) (Ref 31, 52). Additionally, all the presented evidence thus far points toward the enhanced interface forming due to an interaction between the YSZ and amorphous YbDS *during deposition*. Lastly, in Fig. 6(b), at the YSZ/YbDS interface, after thermal exposure there appears to be a new phase/ microstructure within the YSZ, near the YbDS/YSZ

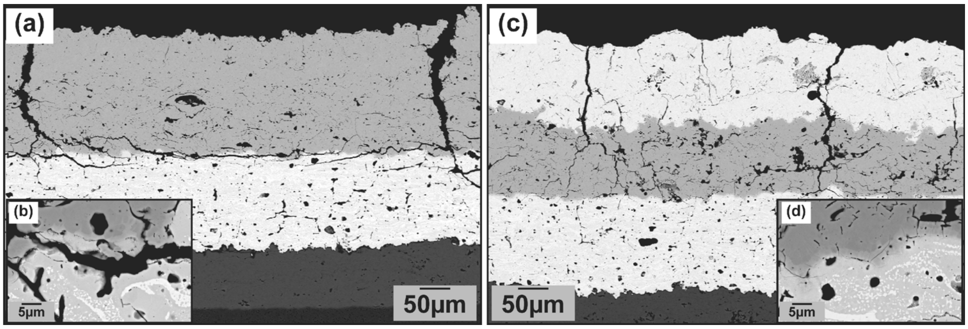

Fig. 7 FCT cross sections of (a, b) Sample B [YbDS amorphous-on-deposition; after 10 20-hour cycles] and (c, d) Sample C [YbDS amorphous-on-deposition; after 10 20-hour cycles] from Table 2. High-magnification images near the YSZ/YbDS interface are shown in both cases

contact zone, which has a unique microstructure compared to the two coatings. This tertiary phase was explored further and will be discussed later in this paper.

Microstructural Analysis of the MultiLayered, MultiMaterial TBCs on YbDS

In the previous section, TBC/EBC interfacial adhesion was shown to be directly influenced by the crystallinity of the EBC before TBC deposition. Here, the effect (if any) of changing the uppermost TBC layer(s) is shown. It is important to reiterate, when the TBC layers were deposited onto crystalline YbDS, none of the MultiLayered systems survived the first heating cycle (Table 4); thus, FCT microstructures of these MultiLayers are not shown here. However, when the TBCs were deposited onto amorphous YbDS, both MultiLayer (YSZ-YSZ and YSZ-GZO) structures survived without evidence during the testing of macroscopic spallation/delamination for the full ten 20-hour cycles. Figure 7 shows the cross-sectional microstructures of these two MultiLayered T-EBCs after 200 hours' thermal cycling at 1300 °C. In the case of the all-YSZ TBC Sample B (Fig. 7a), again the bifurcation of propagating vertical segmentation cracks along the YSZ/YbDS interface can be seen. The morphology of the cracking was almost exactly the same as is seen in Fig. 6(a).

Interestingly, however, in the case of the YSZ/GZO MultiLayered TBC, it seemed there was an appreciably lesser amount of segmentation crack bifurcation compared to the all-YSZ/YbDS T-EBCs. Figure 7(c) serves as a representative image, which illustrates that in the YbDS layer, almost no vertical cracks are seen protruding into the EBC. Nevertheless, similar to the case of the all-YSZ TBCs, the crack opening displacement of the segmentation cracks in the GZO TBC layer(s) appears to have increased somewhat compared to the as-sprayed state (see Fig. 1c). However, the increase in crack opening displacement was not to the extent that was seen in the all-YSZ TBC structures.

The observed differences in the cracking within the EBC layer for the YSZ/GZO T-EBC could indicate the system has undergone different thermomechanical excursions during initial crystallization of the EBC over the first thermal cycle to 1300 °C. However, it can be somewhat ambiguous to identify what drives these excursions to be different.

It has been shown in the literature that the stress state during constrained YbDS crystallization can contribute to 'crack healing' events within the EBC (Ref 50). Figure 1(b) and (c) show in the as-deposited state for both the YSZ-YSZ and YSZ-GZO MultiLayers that the segmentation cracks propagate into the YbDS EBC. However, crack bifurcation after thermal cycling is only seen in Fig. 7(a) with the all-YSZ TBC layers. In both cases in Fig. 7, the YbDS EBC microstructure appears to be comparable—notwithstanding the interface cracks in Fig. 7(a). The exchange of segmented YSZ with segmented GZO alone is not enough to account for the differences in crack bifurcation. Furthermore, there are only slight differences between the segmented YSZ and GZO microstructures (i.e., segmentation crack density), which are also not enough to account for what might be a difference in the stress state that caused bifurcation. This makes ascertaining the quantitative differences in the stress in the EBC for the all-YSZ and YSZ/GZO T-EBCs challenging. Nonetheless, the results presented here are indicative that there is some merit to incorporating GZO into the MultiLayer structure.

Evolution of the YSZ/YbDS Interface During Thermal Cycling

As discussed in Section As-Deposited Microstructural Evaluation, in the as-sprayed state there was some evidence from microstructural and phase/elemental investigations pointing toward the possibility of interexchange of species at the YSZ/YbDS interface during deposition. In traditional thermally-sprayed coatings, especially in the case of bonding between two oxide coatings, the primary mechanism of interlayer adhesion is through mechanical interlocking of successively deposited/quenched droplets (Ref

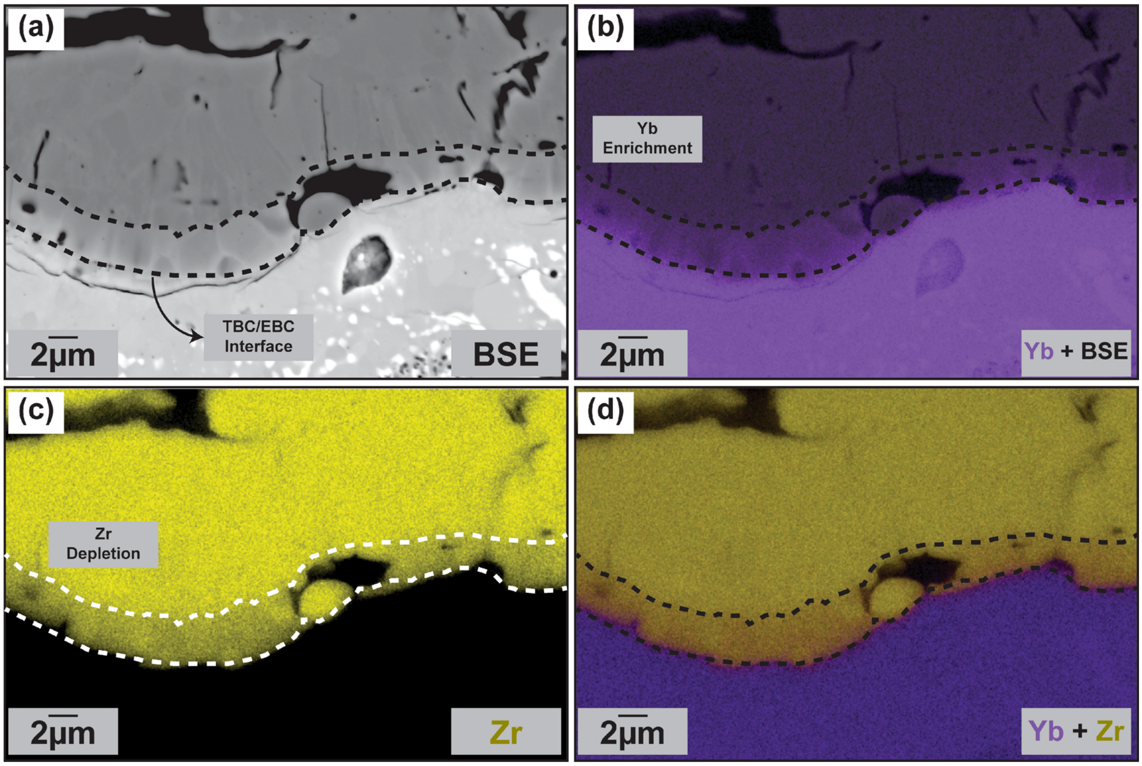

Fig. 8 (a) BSE image of a region of interest between the YSZ/YbDS interface of Sample B [YbDS amorphous-on-deposition] from Table 2 after ten 20-hour thermal cycles at 1300 °C. (b) Yb-M + BSE EDS Map of the same, showing ingression of Yb into the YSZ layer. (c) Zr-L EDS map, showing evidence of depletion of Zr at the interface. (d) Yb-Zr combined EDS map

53, 55). However, this study demonstrates the possibility of an interexchange between ions (i.e., between Yb, Y, and Zr) thereby implying the possibility of an alternative bonding mechanism stronger than mechanical interlocking. In Fig. 6(b), 7(b) and (d), after 200 hours' thermal cycling at 1300°C, there are significant microstructural anomalies at the YSZ/YbDS interface which differ from the as-sprayed state. Furthermore, this unique interface appears irrespective of whether GZO or YSZ is the topmost TBC layer.

Detailed SEM investigations at the interface were carried out to examine these features. Figure 8 shows a representative region of interest at the TBC/EBC interface in TBC Sample B from Table 2 after 200 hours of thermal cycling at 1300 °C. From Fig. 8(a), there is a clear granular structure at the YSZ/YbDS interface, which could not be seen in the as-sprayed state. Using EDS, mapping was conducted to study the presence of Yb, Y, Si, O, and Zr in this region. In the case of Y, Si, and O, there was no clear evidence in the maps of any significant species depletion or enrichment. However, in the case of Yb and Zr, the EDS maps shows some distinctive evidence of Yb ingression and Zr depletion at the YSZ/YbDS interface (see Fig. 8b, c, and d).

Additionally, an EDS line scan was taken at a similar region of interest in Sample C from Table 2 after 200 hours' thermal cycling, shown in Fig. 9. From the Figure, the same granular structure at the YSZ/YbDS interface can be seen once again. Interestingly, the line scan data clearly suggests an onset of zirconium depletion and ytterbium enrichment at the start of this unique region in the BSE image. Furthermore, a local minimum concentration of zirconium and maximum of ytterbium corroborates with the centermost point of one bight granule (indicated by the arrow). It was not possible using this technique to ascertain whether yttrium or silicon were also subjected to concentration migration. Nevertheless, the line scan results clearly suggest there is an interexchange happening between Zr and Yb, which was also suggested in Fig. 8 by the EDS maps.

In some analogous literature, wherein ytterbium thin films are deposited atop fully dense 3YTZ substrates, researchers have found evidence to suggest a mechanism of tracer diffusion between Yb and Zr can occur at temperatures around 1600 K on reasonably short timescales (Ref 64). It is possible that a similar mechanism is occurring in this case of thermal cycling—wherein the temperatures are lower, but the timescales are much longer. Thermodynamically, one can also consider that the concentration gradient of Yb^{3+} between YbDS and YSZ can act as a

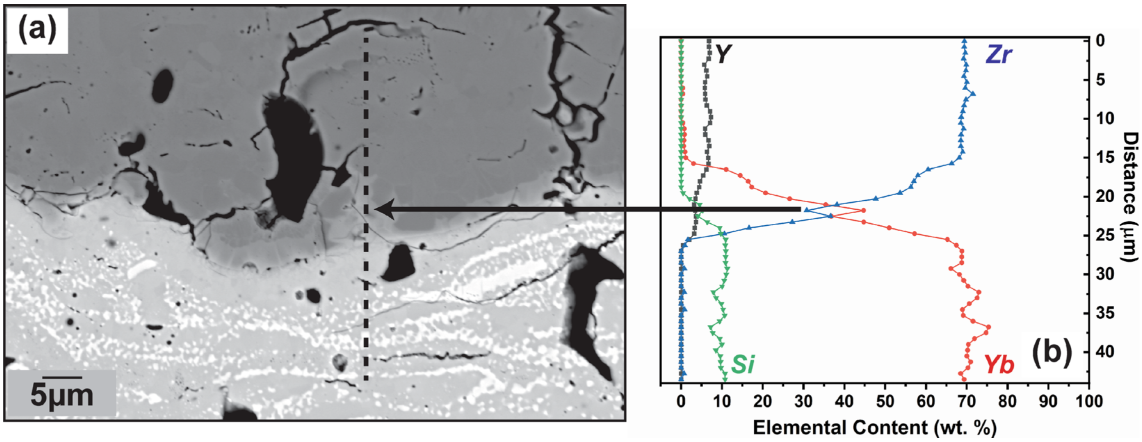

Fig. 9 (a) BSE image of a region of interest between the YSZ/YbDS interface of Sample C from Table 2 after ten 20-hour thermal cycles at 1300 °C. The dashed line indicates the region where an EDS quantitative lines can was taken. (b) shows the extracted elemental compositions for yttrium, silicon, zirconium, and ytterbium from the same linescan. The arrow indicates the region where Zr and Yb interexchange takes place in the BSE image

driver for species migration. In addition, the similarity in ionic radii between Yb^{3+} and Y^{3+} along with the partial-doping of classic 7YSZ can facilitate ingression of Yb^{3+}.

Furthermore, it has been suggested in past literature that diffusion between one material and an amorphous solid can be exacerbated due to the presence of interfacial voids—which act as a type of vacancy site to accelerate the diffusion process (Ref 65, 66). This would be consistent with what was seen in the as-deposited state at the YSZ/YbDS (amorphous) interface—where there were always some amount of interfacial voids (Fig. 1, 2—arrows). Interestingly, these interfacial voids after the 200 hours thermal cycling appear to have almost completely been annihilated, as can be seen in the micrographs of (Fig. 6, 7, 8, and 9). This can simply be due to EBC densification due to high-temperature exposure. However, it is also possible that a similar tracer diffusion mechanism activated by the presence of these voids could be occurring here. To fully investigate this behavior would require highly advanced characterization tools beyond the scope of this paper but are worth noting here as points of interest for future study.

The evidence presented in this study of the possible interexchange between Zr and Yb in plasma-sprayed T-EBCs deposited using traditional means and materials can have significant implications on the efficacy and feasibility of these structures in real turbine components. For instance, if the observed interexchange between ions does indeed take place consistently and reproducibly, it can suggest the presence of a chemical bonding between the YSZ and YbDS, which would thereby supersede the bonding strength of traditional mechanical interlocking of splats (Ref 55, 67, 68). Of future interest would be to study the interaction between APS YSZ and amorphous YbDS on an individual splat level, while concurrently comparing those results with crystalline YbDS. One could then assess differences between the two in the context of (for instance) wetting/contact angle, chemical interactions, etc. Similarly, one could evaluate the interface between as-deposited YSZ and Amorphous YbDS through high-resolution TEM analysis. These investigations are presently underway to address the unanswered questions of what drives the bonding to be sufficiently acceptable to allow these CTE-mismatched layers to coexist (at least to some extent) both after deposition and after thermal cycling.

Conclusions

This study has strived to show the feasibility and efficacy of using traditional and/or conventional, well-known zirconia-based oxides to deposit structurally-stable thermal-environmental barrier coatings solely by air plasma spraying. From the results, it has been shown that despite the high thermal expansion mismatch strains, it is possible for 7YSZ and GZO TBC layers to coexist atop ytterbium disilicate plasma-sprayed EBCs—even after thermal cycling. However, the TBC/EBC bonding was found to be directly influenced by the crystallinity of the EBC before TBC deposition. When spraying the TBC oxides atop crystalline ytterbium silicate, the TBC/EBC bonding was markedly poor—demonstrated in the as-deposited state by appreciably large interfacial cracks. These same TBCs deposited atop crystalline EBCs spalled after a limited number of thermomechanical cycles in FCT.

On the other hand, when the TBC oxides are sprayed atop amorphous ytterbium disilicate, unexpected durability gains were observed that could not be simply explained by (for instance) changes in surface roughness due to EBC crystallization. Rather, a novel interfacial anomaly was observed. Evidence throughout this study suggests that even in the as-sprayed state, TBCs sprayed atop amorphous EBCs may undergo some degree of interexchange of species. In this study, ytterbium and zirconium were found to exhibit evidence of species intermixing in the as-sprayed state, which continued and was seen to progress further during thermal cycling. The resulting microstructures after furnace cycle testing suggested the formation of an interfacial phase with a microstructure that was distinct from both YSZ and ytterbium silicate. Chemical analysis also suggested at these newly formed locations there as an appreciable exchange between Yb and Zr. However, this new phase was only seen after sufficient thermal exposure—and only in the case of the T-EBCs wherein the EBC layer was amorphous prior to the TBC deposition. It is possible that the formation and growth of this new interfacial species contributed to the surprising thermomechanical durability of the T-EBCs seen here.

Nevertheless, this study has shown that it is possible to deposit zirconia-based TBC oxides atop silicate EBCs without inducing catastrophic stresses and fracture events that would render the entire coating useless in a real turbine application. Future works will be carried out to investigate: the possibility of the interdiffusion between ytterbium and zirconium in these systems, the plausibility of a chemical bonding between YSZ and amorphous ytterbium silicate, and the feasibility of these structures in more simulative thermomechanical cycling (i.e., burner rig testing).

Acknowledgments Financial support from the Alexander von Humboldt Foundation during the time of this research is gratefully acknowledged. Sincere thanks to Curtis Johnson for the detailed and insightful discussions during preparation of this manuscript.

Funding Open Access funding enabled and organized by Projekt DEAL.

References

1. L.R. Turcer and N.P. Padture, Towards Multifunctional Thermal Environmental Barrier Coatings (TEBCs) Based on Rare-Earth Pyrosilicate Solid-Solution Ceramics, *Scr. Mater.*, 2018, **154**, p 111-117.
2. M. Schnieder, T. Sommer, Turbines for Industrial Gas Turbine Systems, Modern Gas Systems: High Efficiency, Low Emission, Fuel Flexible Power Generationed., P. Jahnson, Ed., Woodhead Publishing Limited (2013).
3. M. Konter, H.P. Bossmann, Materials and Coatings Development for Gas Turbine Systems and Components, Modern Gas Turbine Systems: High Efficiency, Low Emission, Fuel Flexible Power Generationed., P. Jahnson, Ed., Woodhead Publishing Limited (2013).
4. P. Chiesa, G. Lozza and L. Mazzocchi, Using Hydrogen as Gas Turbine Fuel, *J. Eng. Gas Turbines Power*, 2005, **127**(1), p 73-80.
5. E. Bancalari, P. Chan, I.S. Diakunchak, Advanced Hydrogen Gas Turbine Development Program, pp. 977-987 (2007).
6. D. LaChapelle, M. Noe, W. Edmondson, H. Stegemiller, J. Steibel, D. Chang, CMC Materials Applications to Gas Turbine Hot Section Components, p 3266 (1998).
7. C.P. Beesley, The Application of CMCs in High Integrity Gas Turbine Engines, *Key Eng. Mater.*, 1997, **1**(127), p 165-176.
8. P. Spriet, CMC Applications to Gas Turbines, Ceramic Matrix Compositesed., p 591-608 (2014).
9. J. Steibel, Ceramic Matrix Composites Taking Flight at Ge Aviation, *Am. Ceram. Soc. Bull.*, 2019, **98**(3), p 30-33.
10. R.C. Robinson and J.L. Smialek, SiC Recession Caused by SiO2 Scale Volatility under Combustion Conditions: I, Experimental Results and Empirical Model, *J. Am. Ceram. Soc.*, 1999, **82**(7), p 1817-1825.
11. K.L. More, P.F. Tortorelli, L.R. Walker, N. Miriyala, J.R. Price and M. van Roode, High- Temperature Stability of SiC-Based Composites in High-Water-Vapor-Pressure Environments, *J. Am. Ceram. Soc.*, 2003, **86**(8), p 1272-1281.
12. L.U.J.T. Ogbuji, Oxidative Pest Degradation of Hi-Nicalon/BN/SiC Composite as a Function of Temperature and Time in the Burner Rig, 23rd Annual Conference on Composites, Advanced Ceramics, Materials, and Structures: B: Ceramic Engineering and Science Proceedings ed., p 105-114 (1999).
13. G.N. Morscher, J. Hurst and D. Brewer, Intermediate-Temperature Stress Rupture of a Woven Hi-Nicalon, BN-Interphase, SiC-Matrix Composite in Air, *J. Am. Ceram. Soc.*, 2000, **83**(6), p 1441-1449.
14. J.A. DiCarlo, H.M. Yun, G.N. Morscher, R.T. Bhatt, SiC/SiC Composites for 1200°C and Above, Handbook of Ceramic Compositesed., N.P. Bansal, Ed., Springer US, p 77-98 (2005).
15. N.S. Jacobson, E.J. Opila and K.N. Lee, Oxidation and corrosion of ceramics and ceramic matrix composites, *Curr. Opin. Solid State Mater. Sci.*, 2001, **5**(4), p 301-309.
16. K.N. Lee, D.S. Fox and N.P. Bansal, Rare earth silicate environmental barrier coatings for SiC/SiC composites and Si3N4 ceramics, *J. Eur. Ceram. Soc.*, 2005, **25**(10), p 1705-1715.
17. I. Spitsberg and J. Steibel, Thermal and Environmental Barrier Coatings for SiC/SiC CMCs in Aircraft Engine Applications*, *Int. J. Appl. Ceram. Tech.*, 2004, **1**(4), p 291-301.
18. N.S. Jacobson, J.L. Smialek, D.S. Fox, E.J. Opila, Durability of silica-protected ceramics in combustion atmospheres, (1995).
19. K.N. Lee, Environmental Barrier Coatings for SiCf/SiC, Ceramic Matrix Compositesed., p 430-451 (2014).
20. B.T. Richards and H.N.G. Wadley, Plasma spray deposition of tri-layer environmental barrier coatings, *J. Eur. Ceram. Soc.*, 2014, **34**(12), p 3069-3083.
21. E. Bakan, D. Marcano, D. Zhou, Y.J. Sohn, G. Mauer, and R. Vaßen, Yb2Si2O7 Environmental Barrier Coatings Deposited by

Various Thermal Spray Techniques: A Preliminary Comparative Study, *J. Therm. Spray Technol.*, 2017, **26**(6), p 1011-1024.

22. Y. Xu, X. Hu, F. Xu and K. Li, Rare Earth Silicate Environmental Barrier Coatings: Present Status and Prospective, *Ceram. Int.*, 2017, **43**(8), p 5847-5855.
23. E. Bakan, Y.J. Sohn, W. Kunz, H. Klemm and R. Vaßen, Effect of Processing on High-Velocity Water Vapor Recession Behavior of Yb-Silicate Environmental Barrier Coatings, *J. Eur. Ceram. Soc.*, 2019, **39**(4), p 1507-1513.
24. E. Garcia, H. Lee and S. Sampath, Phase and Microstructure Evolution in Plasma Sprayed Yb2Si2O7 Coatings, *J. Eur. Ceram. Soc.*, 2019, **39**(4), p 1477-1486.
25. J.A. Deijkers and H.N.G. Wadley, Hafnium Silicate Formation During Oxidation of a Permeable Silicon + HfO2 Powder Composite System, *Acta Mater.*, 2020, **201**, p 448-461.
26. B.J. Harder, Oxidation Performance of Si-HfO2 Environmental Barrier Coating Bond Coats Deposited Via Plasma Spray-Physical Vapor Deposition, *Surf. Coat. Technol.*, 2020, **384**, p 125311.
27. E. Bakan, Y.J. Sohn and R. Vaßen, Microstructure and Phase Composition Evolution of Silicon- Hafnia Feedstock During Plasma Spraying and Following Cyclic Oxidation, *Acta Mater.*, 2021, **214**, p 117007.
28. D. Zhu, K.N. Lee, R.A. Miller, Thermal Conductivity and Thermal Gradient Cyclic Behavior of Refractory Silicate Coatings on Sic/Sic Ceramic Matrix Composites, 25th Annual Conference on Composites, Advanced Ceramics, Materials, and Structures: B: Ceramic Engineering and Science Proceedings ed., p 443-452 (2001).
29. N. Al Nasiri, N. Patra, D. Horlait, D.D. Jayaseelan and W.E. Lee, Thermal Properties of Rare- Earth Monosilicates for EBC on Si-Based Ceramic Composites, *J. Am. Ceram. Soc.*, 2016, **99**(2), p 589-596.
30. D.H. Olson, J.A. Deijkers, K. Quiambao-Tomko, J.T. Gaskins, B.T. Richards, E.J. Opila, P.E. Hopkins and H.N.G. Wadley, Evolution of Microstructure and Thermal Conductivity of Multifunctional Environmental Barrier Coating Systems, *Mater. Today Phys.*, 2021, **17**, p 100304.
31. S.V. Shinde and S. Sampath, Interplay Between Cracking and Delamination in Incrementally Deposited Plasma Sprayed Coatings, *Acta Mater.*, 2021, **215**, p 117074.
32. S.V. Shinde, S. Sampath, Factors Governing Segmentation Crack Characteristics in Air Plasma Sprayed Ceramics, (2021).
33. J.W. Hutchinson and Z. Suo, Mixed Mode Cracking in Layered Materials, *Adv. Appl. Mech.*, 1991, **29**, p 63-191.
34. A.G. Evans and J.W. Hutchinson, The Mechanics of Coating Delamination in Thermal Gradients, *Surf. Coat. Technol.*, 2007, **201**(18), p 7905-7916.
35. M.D. Thouless, E. Olsson and A. Gupta, Cracking of Brittle Films on Elastic Substrates, *AcM&M*, 1992, **40**(6), p 1287-1292.
36. D. Zhu, R. Miller, D. Fox, Thermal and Environmental Barrier Coating Development for Advanced Propulsion Engine Systems, 48th AIAA/ASME/ASCE/AHS/ASC Structures, Structural Dynamics, and Materials Conference, 2007, American Institute of Aeronautics and Astronautics (2007)
37. D. Zhu, Aerospace Ceramic Materials: Thermal, Environmental Barrier Coatings and SiC/SiC Ceramic Matrix Composites for Turbine Engine Applications, (2018)
38. J. Zhong, D. Yang, S. Guo, X. Zhang, X. Liang, X. Wu, Rear Earth Oxide Multilayer Deposited by Plasma Spray-Physical Vapor Deposition for Envisaged Application as Thermal/Environmental Barrier Coating, Coatings ed., (2021)
39. J.A. Krogstad, S. Krämer, D.M. Lipkin, C.A. Johnson, D.R.G. Mitchell, J.M. Cairney and C.G. Levi, Phase Stability of t′-Zirconia-Based Thermal Barrier Coatings: Mechanistic Insights, *J. Am. Ceram. Soc.*, 2011, **94**(s1), p s168-s177.
40. J.A. Krogstad, S. Krämer, D.M. Lipkin, C.A. Johnson, D.R. Mitchell, J.M. Cairney and C.G. Levi, Phase stability of t′-zirconia-based thermal barrier coatings: mechanistic insights, *J. Am. Ceram. Soc.*, 2011, **94**, p s168-s177.
41. E.J. Gildersleeve and S. Sampath, Dynamic Interactions of Ingested Molten Silicate Particles with Air Plasma Sprayed Thermal Barrier Coatings, *JMatR*, 2020, **35**(17), p 2321-2334.
42. E.J. V Gildersleeve, V. Viswanathan and S. Sampath, Molten Silicate Interactions with Plasma Sprayed Thermal Barrier Coatings: Role of Materials and Microstructure, *J. Eur. Ceram. Soc.*, 2019, **39**(6), p 2122-2131.
43. V. Viswanathan, G. Dwivedi and S. Sampath, Engineered Multilayer Thermal Barrier Coatings for Enhanced Durability and Functional Performance, *J. Am. Ceram. Soc.*, 2014, **97**(9), p 2770-2778.
44. V. Viswanathan, G. Dwivedi and S. Sampath, Multilayer, Multimaterial Thermal Barrier Coating Systems: Design, Synthesis, and Performance Assessment, *J. Am. Ceram. Soc.*, 2015, **98**(6), p 1769-1777.
45. R. Vaßen, F. Traeger and D. Stöver, New Thermal Barrier Coatings Based on Pyrochlore/YSZ Double-Layer Systems, *Int. J. Appl. Ceram. Tech.*, 2004, **1**(4), p 351-361.
46. R. Vaßen, E. Bakan, D. Mack, S. Schwartz-Lückge, D. Sebold, Y. Jung Sohn, D. Zhou and O. Guillon, Performance of YSZ and Gd2Zr2O7/YSZ Double Layer Thermal Barrier Coatings in Burner Rig Tests, *J. Eur. Ceram. Soc.*, 2020, **40**(2), p 480-490.
47. E. Bakan, Y.J. Sohn and R. Vaßen, Metastable to Stable Phase Transformation in Atmospheric Plasma Sprayed Yb-Silicate Coating During Post-Heat Treatment, *Scripta Mater.*, 2023, **225**, p 115169.
48. E.J. V Gildersleeve and S. Sampath, Durability of Plasma Sprayed Thermal Barrier Coatings with Controlled Properties Part I: For Planar Disk Substrates, *Surf. Coat. Technol.*, 2021, **424**, p 127678.
49. R. Vaßen, E. Bakan, D. Sebold and Y.J. Sohn, Correlation of Process Conditions, Porosity Levels and Crystallinity in Atmospherically Plasma Sprayed Yb2Si2O7 Environmental Barrier Coatings, *J. Compos. Sci.*, 2021, **5**(8), p 198.
50. E. Bakan and R. Vaßen, Crack healing mechanisms in atmospheric plasma sprayed Yb-silicate coatings during post-process heat treatment, *J. Eur. Ceram. Soc.*, 2023, **43**(8), p 3684-3693.
51. D. Lal, J. Saputo, E.J. Van Gildersleeve and S. Sampath, Through Thickness Changes to Stiffness and Thermal Conductivity in Thermal Barrier Coatings Subjected to Gradient Exposure, *J. Eur. Ceram. Soc.*, 2023, **43**(9), p 4146-4152.
52. J.W. Hutchinson, Mixed Mode Fracture Mechanics of Interfaces, Metal-Ceramic Interfaces, A.G.E. M. Rühle, M. F. Ashby, J.P. Hirth Ed., Pergamon Press Oxford, pp. 295-306 (1990)
53. S. Sampath, U. Schulz, M.O. Jarligo and S. Kuroda, Processing Science of Advanced Thermal-Barrier Systems, *MRS Bull.*, 2012, **37**(10), p 903-910.
54. H. Herman, Plasma Spray Deposition Processes, *MRS Bull.*, 1988, **13**(12), p 60-67.
55. S. Sampath and H. Herman, Rapid Solidification and Microstructure Development During Plasma Spray Deposition, *J. Therm. Spray Technol.*, 1996, **5**(4), p 445-456.
56. S. Shinde and S. Sampath, A Critical Analysis of the Tensile Adhesion Test for Thermally Sprayed Coatings, *J. Therm. Spray Technol.*, 2022, **31**(8), p 2247-2279.
57. V. Lughi and D.R. Clarke, High Temperature Aging of YSZ Coatings and Subsequent Transformation at Low Temperature, *Surf. Coat. Technol.*, 2005, **200**(5), p 1287-1291.
58. C. Mercer, J.R. Williams, D.R. Clarke and A.G. Evans, On a Ferroelastic Mechanism Governing the Toughness of Metastable Tetragonal-Prime (t′) Yttria-Stabilized Zirconia, *Proceed. R. Soc. A Math. Phys. Eng. Sci.*, 2007, **463**(2081), p 1393-1408.

59. M. Roskosz, M.J. Toplis and P. Richet, Crystallization of Highly Supercooled Silicate Melts, *Adv. Eng. Mater.*, 2006, **8**(12), p 1224-1228.
60. O.N. Koroleva, The Structure of Lithium Silicate Melts Revealed by High-Temperature Raman Spectroscopy, *Spectrosc. Lett.*, 2017, **50**(5), p 257-264.
61. E. Garcia, O. Sotelo-Mazon, C.A. Poblano-Salas, G. Trapaga and S. Sampath, Characterization of Yb2Si2O7-Yb2SiO5 Composite Environmental Barrier Coatings Resultant from in situ Plasma Spray Processing, *Ceram. Int.*, 2020, **46**(13), p 21328-21335.
62. E. Garcia, H.F. Garces, L.R. Turcer, H. Bale, N.P. Padture and S. Sampath, Crystallization Behavior of Air-Plasma-Sprayed Ytterbium-Silicate-Based Environmental Barrier Coatings, *J. Eur. Ceram. Soc.*, 2021, **41**(6), p 3696-3705.
63. J.A. Deijkers, M.R. Begley and H.N.G. Wadley, Failure Mechanisms in Model Thermal and Environmental Barrier Coating Systems, *J. Eur. Ceram. Soc.*, 2022, **42**(12), p 5129-5144.
64. S. Swaroop, M. Kilo, C. Argirusis, G. Borchardt and A.H. Chokshi, Lattice and Grain Boundary Diffusion of Cations in 3YTZ Analyzed Using SIMS, *Acta Mater.*, 2005, **53**(19), p 4975-4985.
65. R.H. Doremus, Ionic Transport in Amorphous Oxides, *JElS*, 1968, **115**(2), p 181.
66. J. Horváth, J. Ott, K. Pfahler and W. Ulfert, Tracer Diffusion in Amorphous Alloys, *MSEng*, 1988, **97**, p 409-413.
67. T. Narusawa, S. Komiya and A. Hiraki, Diffuse Interface in Si (substrate)-Au (Evaporated Film) System, *Appl. Phys. Lett.*, 2003, **22**(8), p 389-390.
68. H. Weiss, Adhesion of Advanced Overlay Coatings: Mechanisms and Quantitative Assessment, *Surf. Coat. Technol.*, 1995, **71**(2), p 201-207.